Insight into synergistic effect of Ti$_3$C$_2$ MXene and MoS$_2$ on anti-photocorrosion and photocatalytic of CdS for hydrogen production

Chao Wu [1], Weixin Huang [1], Huanmin Liu, Kangle Lv, Qin Li [*]

Key Laboratory of Catalysis and Energy Materials Chemistry of Ministry of Education & Hubei Key Laboratory of Catalysis and Materials Science & Key Laboratory of Analytical Chemistry of the State Ethnic Affairs Commission, South-Central Minzu University, Wuhan 430074, China

ARTICLE INFO

ABSTRACT

Facing the increasingly serious issues of energy crisis and environmental pollution, it is vital to develop efficient and durable photocatalysis systems for hydrogen (H$_2$) production from water splitting. However, for the famous CdS-based systems, the bottleneck of poor efficiency and low stability arisen from photocorrosion has not been broken through yet. In this study, a ternary composite of CdS, MoS$_2$ and Ti$_3$C$_2$ MXene with intimately contact interfaces was successfully constructed via an in situ growth method, which exhibited reinforced photocatalytic H$_2$-production activity and increased photocorrosion resistant capability. Both of experimental characterizations and density functional theory (DFT) calculations well proved that the photogenerated holes and electrons of CdS timely migrated to Ti$_3$C$_2$ and MoS$_2$, respectively. As a consequence, the optimal sample displayed a high H$_2$ production rate of 14.88 mmol·h^{-1}·g^{-1} with a lifetime of up to 78 h, and the component and structure of the composite were kept intact during the photocatalysis reaction. This work highlights the synergistic effect of the Ti$_3$C$_2$ MXene and MoS$_2$ as redox dual cocatalysts on the promoted photocatalytic performance and durability of CdS, which can be anticipated to significantly enhance the commercial availability of CdS and even boost its incorporation into industrial applications.

1. Introduction

The ever-increasing environmental pollution and energy shortage caused by the rapid consumption of fossil fuels have become serious threat to human society. Employing semiconductor materials to capture solar energy and photocatalyze water decomposition to produce green and sustainbale hydrogen (H$_2$) is expected to alleviate these crises [1–5]. In general, an ideal photocatalyst with outstanding performance and stability needs to meet following requirements: (i) The photocatalyst has excellent light absorption properties to capture solar energy; (ii) The photo-generated charge carriers from semiconductors can migrate and separate effectively; (iii) The band structure of the photocatalyst is suitable for reducing H$_2$O into H$_2$ [6–9].

Nanosized cadmium sulfide (CdS) is regarded as a promising H$_2$-production photocatalyst due to its suitable band gap (2.4 eV), negative enough conduction band (CB) position (−0.58 eV) and visible light absorption capacity [10–12], which satisfies the above requirements (i) and (iii). However, the agglomerate of CdS nanoparticles in the growth process poses a significant obstacle for meeting the requirement (ii)
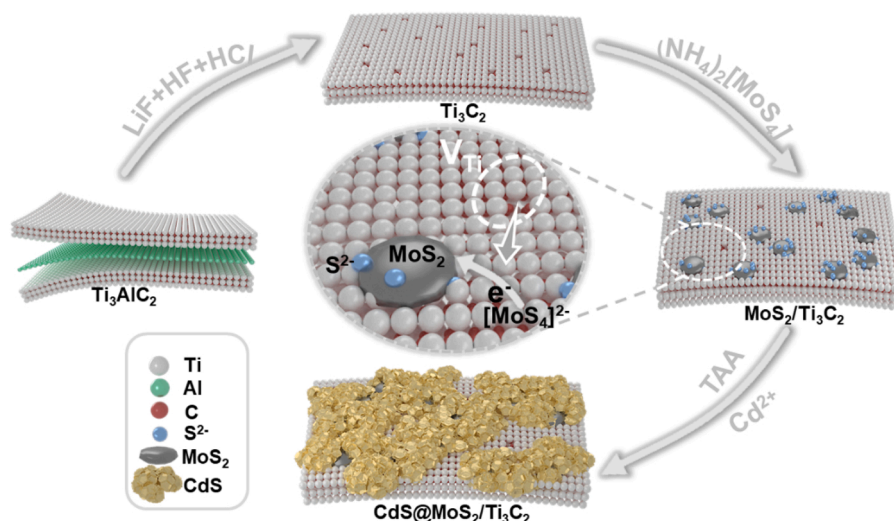
because it results in rapid charge carrier recombination and significant depletion in the amount of surface active sites [13–15]. Of greater concern, photocorrosion susceptibility of bare CdS usually led to poor H$_2$-production efficiency and low photocatalytic stability [16–18]. The causation behind this photocorrosion process of CdS was based on the oxidation of lattice sulfur of CdS by photogenerated holes, synchronously accompanied by the reduction of Cd^{2+} to metallic Cd by photogenerated electrons [19]. As a result, the nanostructure of CdS was seriously damaged, which greatly lowered the photocatalytic performance and lifetime. The major challenge in further development and extensive application of CdS-based composites lies on how to enhance their photocatalytic activity and prevent them from photocorrosion.

To address the above issues, one common strategy is to load particular cocatalysts on CdS photocatalyst to timely transfer the photogenerated charges away from its surface. [20–24]. For example, molybdenum disulfide (MoS$_2$), with lamellar S-Mo-S structure stacked together by weak van der Waals interactions, is a splendid reductive cocatalyst for trapping photogenerated electrons, whose sulfur edges can provide abundant active sites for proton reduction [25–27].

Scheme 1. Schematic illustration of the preparation procedure of the CdS@MoS$_2$/Ti$_3$C$_2$ composite.

Previously, Han et al. used sodium molybdate (Na$_2$MoO$_4$) and thio-noacetamide (TAA) to introduce MoS$_2$ onto CdS via a high-temperature hydrothermal method [28]. Ma et al. utilized ammonium molybdate ((NH$_4$)$_2$MoO$_4$) and S powder to form MoS$_2$ through thermal decomposition, and then added extra CdS to construct CdS/MoS$_2$ heterostructure [29]. However, these methods for preparing MoS$_2$/CdS composites required relatively harsh conditions of high temperature or pressure and sometimes produced toxic H$_2$S gas, which were tedious, environmentally harmful and highly energy-consuming [7,30,31]. An alternative method to establish the MoS$_2$-based composites is reducing the (NH$_4$)$_2$MoS$_4$ precursor into MoS$_2$ by photogenerated electrons of semiconductors ([MoS$_4$]$^{2-}$ + 2e$^-$ → MoS$_2$ + 2S^{2-}) [7,32]. In this way, direct reduction of molybdenum salt by photogenerated electrons enables MoS$_2$ to be tightly coupled to the semiconductor, which promotes interfacial charge transfer and shortens the electron transfer path from the semiconductor to MoS$_2$.

Another attractive candidate of cocatalyst for photocatalytic H$_2$ production is two-dimensional (2D) titanium carbide (Ti$_3$C$_2$) MXene [8,33,34]. Since its first discovery in 2011 by etching Ti$_3$AlC$_2$, Ti$_3$C$_2$ MXene has garnered much attention for its unique electrical, optical and thermodynamic properties in many scientific fields including photocatalysis [35–40]. It is worth mentioning that, during the preparation of 2D Ti$_3$C$_2$, the etching agent would inevitably remove some Ti atoms on the surface to form Ti vacancies, which are rich in electrons and show strong reducibility to in situ reduce some metal salts [10,41]. Moreover, it had been reported that Ti$_3$C$_2$ MXene could act as a hole mediator, making the holes flow from the semiconductor to itself [42,43]. However, it is rarely noted that Ti$_3$C$_2$ and MoS$_2$ could be coupled via a self-reduction method to cooperatively reinforce the photoactivity and photostability of CdS.

Herein, as shown in Scheme 1, MoS$_2$ was decorated in situ on the 2D Ti$_3$C$_2$ nanosheets through direct reduction of (NH$_4$)$_2$MoS$_4$ at the sites of reductive Ti vacancies (V$_{Ti}$). Then, the generated S^{2-} ions reacted with the added Cd^{2+} to make CdS nucleate and grow near MoS$_2$, and the residual Cd^{2+} ions were reacted with thioacetamide (TAA) via microwave hydrothermal treatment to form outer-layered CdS. Finally, ternary CdS@MoS$_2$/Ti$_3$C$_2$ (CTM) nanocomposites with intimate contact interface were successfully obtained. The experimental and theoretical calculation results comprehensively proved that the co-catalytic modification of Ti$_3$C$_2$ and MoS$_2$ not only promoted the separation of photogenerated charge carriers on the surface of CdS, but also successfully inhibited the photocorrosion reactions to a great extent.

2. Experimental section

2.1. Preparation of 2D Ti$_3$C$_2$ nanosheets

The 2D ultrathin Ti$_3$C$_2$ nanosheets were synthesized by a freeze-and-thaw method based on a previously reported literature [44]. Typically, 37 mL of 9 M hydrochloric acid (HCl, Sinopharm, ≥ 99.8%) aqueous solution was blended with 4 mL of hydrofluoric acid (HF, Sinopharm) solution (40%) to form a mixed acid solution, and then 1.6 g of lithium fluoride (LiF, Aladdin, 99%) was added in the solution and stirred at room temperature for 10 min. After that, 1 g of Ti$_3$AlC$_2$ (11 Tecnology, 98%) was carefully and slowly added into the above solution in 5 min, avoiding local overheating. The mixture was placed in an oil bath at 35 °C, and the etching reaction lasted for 24 h. Thereafter, the product was washed with deionized (DI) water until the pH value of the filtrate was larger than 6, and then the product was dried in vacuum at 60 °C for 12 h.

The prepared power (1.5 g) was well dispersed into 100 mL of DI water to be a homogeneous suspension. Subsequently, it was put in a refrigerator (−20 °C) until it was completely frozen, and then naturally thawed at room temperature. After repeating the above freeze-and-thaw process for five times, the thawy suspension was sonicated for 30 min in an ice bath. Finally, the ultrathin Ti$_3$C$_2$ nanosheets were obtained by centrifugating at 3500 rpm for 30 min and freeze drying the supernatant.

2.2. Preparation of MoS$_2$/Ti$_3$C$_2$ composite

The MoS$_2$/Ti$_3$C$_2$ composite was prepared by a self-reduction method. Typically, 6.2 mg of Ti$_3$C$_2$ was dispersed in 3 mL of DI water, and thoroughly mixed to obtain a uniform suspension. Meanwhile, 0.9 mg of ammonium tetrathiomolybdate ((NH$_4$)$_2$MoS$_4$, Aladdin, 99.95%) was dissolved in 25 mL of DI water, and then, the solution was slowly added to the above Ti$_3$C$_2$ suspension and stirred at room temperature for 1 h. The resulted sediment was alternately washed with DI water and ethanol for several times. Finally, the MoS$_2$/Ti$_3$C$_2$-9 composite (denoted as TM9) was obtained after the freeze-drying treatment, where the 9 (unit: wt.%) refers to the theoretical mass percentage of MoS$_2$ to Ti$_3$C$_2$.

2.3. Preparation of CdS@MoS$_2$/Ti$_3$C$_2$ composites

The CdS@MoS$_2$/Ti$_3$C$_2$ composites were synthesized by a microwave-hydrothermal method. In detail, cadmium acetate dihydrate (Cd(CH$_3$COO)$_2$·2 H$_2$O, Sinopharm, ≥ 98%) (1.7192 g) was added to the
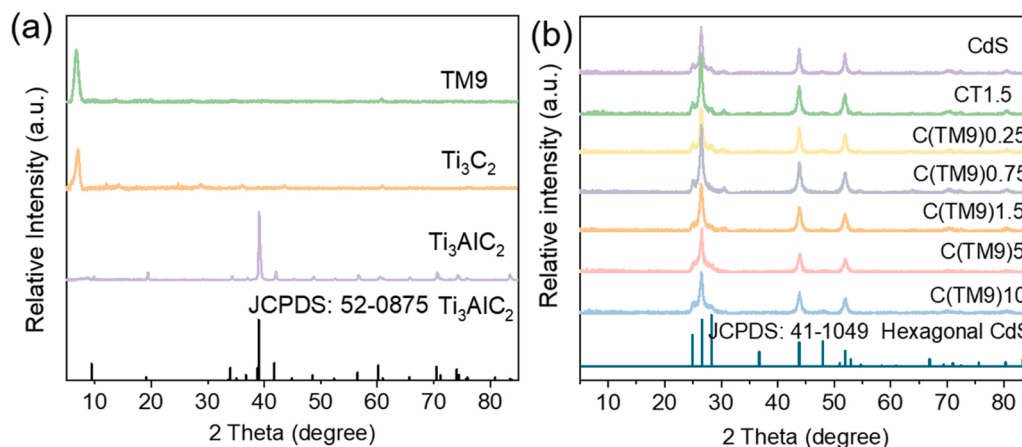
Fig. 1. (a) XRD patterns of the Ti_3AlC_2, Ti_3C_2 and TM9 samples. (b) XRD patterns of CdS, CT1.5 and C(TM9)x samples.

TM9 suspension (25 mL) and stirred for 30 min at room temperature, followed by adding 0.9692 g of TAA (C_2H_5NS, Sinopharm, $\geq$ 99.0%) and stirring for another 30 min. After that, the uniform mixture was transferred to a microwave autoclave (100 mL) and heated at 180 ℃ for 45 min. When cooled to room temperature, the product was washed with DI water and ethanol until the pH value of the filtrate was larger than 6, and then dried under vacuum at 60 ℃ for 12 h. The as-prepared $CdS@MoS_2/Ti_3C_2$ composites were named as C(TM9)x (x = 0.25, 0.75, 1.5, 5, and 10), where x refers to the theoretical mass percentage of TM9 to CdS. For comparison, the binary $CdS@Ti_3C_2$ (i.e. C(TM0)1.5, denoted as CT1.5 for short) and bare CdS were prepared under the same experimental conditions without adding MoS_2 and MoS_2/Ti_3C_2, respectively.

2.4. Preparation of CdS/MoS₂

The CdS/MoS_2 composite was fabricated by a photodeposition method. Typically, 100 mg of the as-prepared CdS was dispersed in 100 mL of DI water, and then 2.28 mL of $(NH_4)_2MoS_4$ aqueous solution (0.1 mg/mL) was added in it and stirred for 10 min at room temperature. The mixture solution was irradiated by a xenon lamp (300 W) under continuous stirring for 5 min, and finally the CdS/MoS_2 composite was obtained through vacuum filtering and washing by DI water and drying in vacuum, which was denoted as the CM0.14 sample since the theoretical mass percentage of MoS_2 to CdS was 0.14 wt.%.

2.5. Characterizations

The crystal structure of the catalysts were identified by powder X-ray diffraction (XRD, D8 Advance, Bruker) with a monochrome Cu Kα generator ($\lambda = 1.5406$ Å). Raman spectra were obtained by laser confocal Raman spectrometer (Thermo Fisher Scientific, DXR 2xi) to confirm the presence of MoS_2. X-ray photoelectron spectroscopy (XPS) was tested on the Escalab 250xi spectrometer (Thermo Scientific). The actual mass percentages of Ti_3C_2 and MoS_2 in the samples were characterized by inductively coupled plasma-optical emission spectroscopy (ICP-OES, Prodigy 7 spectrometer, Leeman Labs Inc.). The morphology of the samples was observed by transmission electron microscopy (TEM, Talos F200S, Thermo Scientific), field emission scanning electron microscope (FESEM, SU8010, Hitachi), and high angle ring dark field scanning/transmission electron microscope (HAADF-STEM, Talos F200S, Thermo Scientific). The elemental composition of the samples was analyzed by energy dispersive spectroscopy (EDS, linked to HAADF-STEM). UV–visible diffuse reflectance spectroscopy (UV-vis DRS) was measured on an UV–visible spectrophotometer (UV2550, Shimadzu). Photoluminescence (PL) spectra were obtained using a fluorescence spectrophotometer (F-7000, Hitachi), with an excitation wavelength of 270 nm.

2.6. Photocatalytic H₂ production

The photocatalytic performance of the samples was investigated via testing H_2 production efficiency in an automatic online trace gas analysis system (Labsolar-6A, Beijing Perfect Light Technology Co., Ltd.). A xenon lamp (300 W) with a 420 nm cut-off filter was used as the light source. The illumination area was ca. 33 cm^2, and the bulb was nine centimeters away from the top of the reaction solution. Before the hydrogen reaction, the 20 mg of the photocatalyst samples were uniformly dispersed in 80 mL of lactic acid (LA) aqueous solution (10 v%). During the photocatalytic reaction, 0.6 mL of the produced gas (H_2) was automatically collected every hour and injected into a gas chromatography (GC-2018, Shimazu, with TCD with 5 Å molecular sieve column, with N_2 as the carrier gas).

2.7. Photoelectrochemical measurements

Photoelectrochemical properties of the samples, including the transient photocurrent responses (TPR), electrochemical impedance spectroscopy (EIS) and linear sweep voltammetry curves (LSV), were characterized on CHI760e electrochemical workstation (Shanghai Chenhua, China) with a standard three-electrode system, where the reference electrode and counter electrode were Ag/AgCl in the saturated KCl solution and Pt wire, respectively, and the working electrode was the sample coated fluorine-doped tin oxide glass (FTO glass). The specific preparation of the working electrode has been reported in our previous work [39]. During the measurements, the aqueous solution of 0.5 M Na_2SO_4 (pH = 5.45) was used as the electrolyte, and 420 nm-LED was served as light source.

2.8. Computational method

The density functional theory (DFT) calculations were carried out using the Vienna ab initio Simulation Package (VASP) with the projector augment wave method. Generalized gradient approximation of the Perdew-Burke-Ernzerhof (PBE) functional was utilized. The cutoff energy was 500 eV, and structure relaxation was performed till the energy and force convergence criteria respectively reached 1×10^{-5} eV and 0.02 eV Å^{-1}. The vacuum layer was set as 15 Å. The van der Waals interaction was amended by the DFT-D3 method of Grimme [45].

3. Results and discussion

3.1. Phase structure and component

The crystal phase and the components of the as-prepared samples were comprehensively analyzed by the characterizations of XRD, Raman
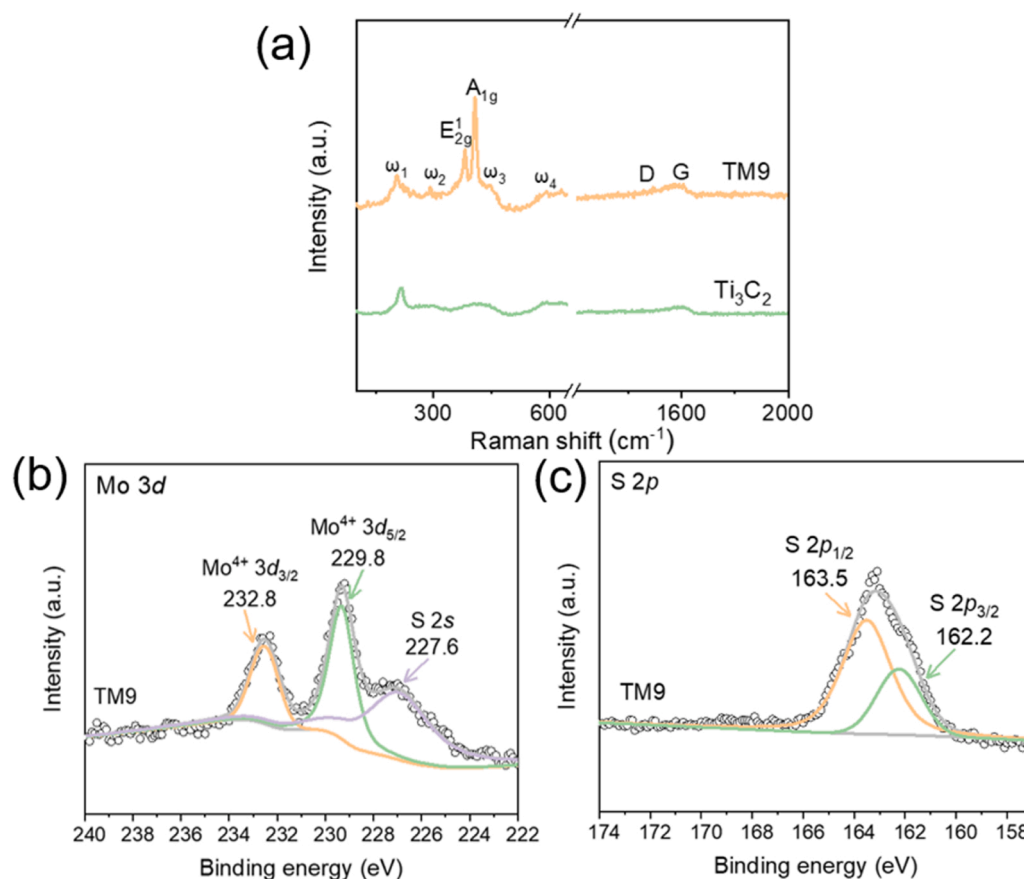
Fig. 2. (a) Raman spectra of TM9 sample. High-resolution XPS spectra of (b) Mo 3*d* and (b) S 2*p* of of TM9 sample.
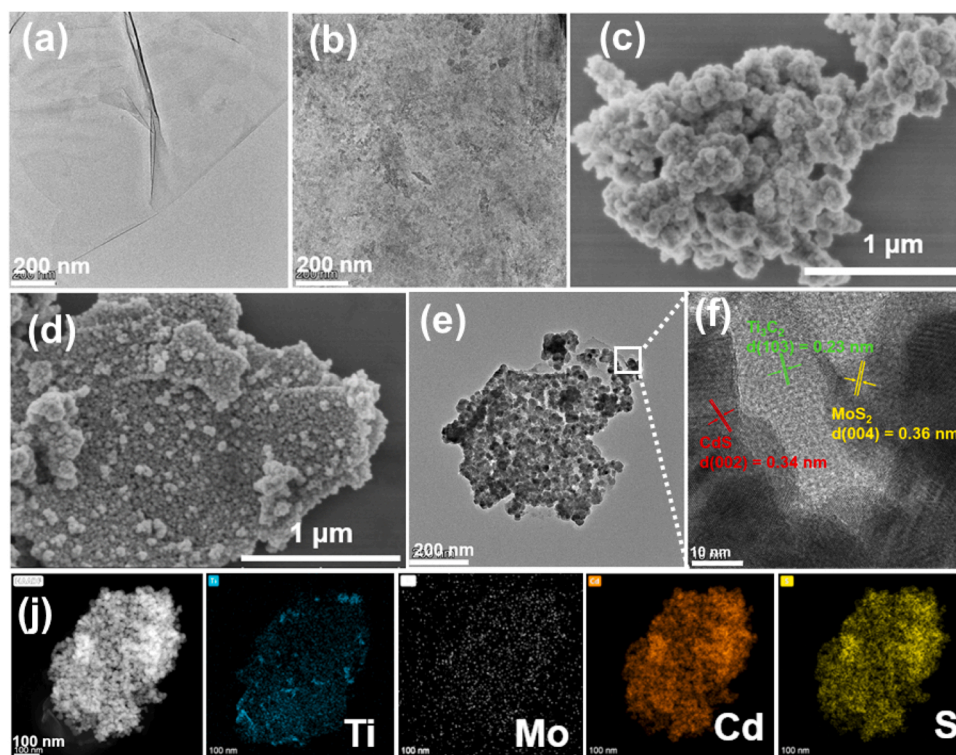

Fig. 3. TEM images of (a)Ti$_3$C$_2$ and (b) TM9 samples. FESEM images of (c) CdS and (d) C(TM9)1.5 samples. (e) TEM and (f) HRTEM images of C(TM9)1.5 sample. (j) HAADF-STEM image of the C(TM9)1.5 sample and the EDS mapping images of its Ti, Mo, Cd, and S atoms.
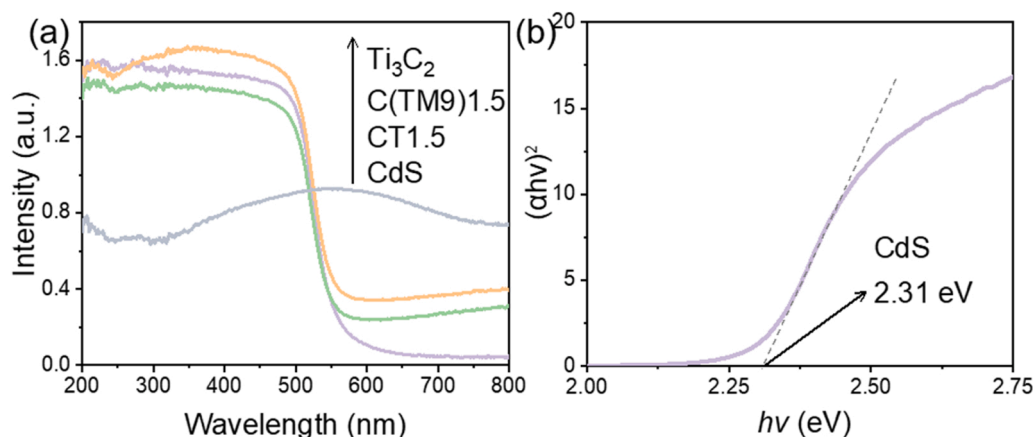
Fig. 4. (a) DRS spectra of CdS, CT1.5 and C(TM9)1.5 samples and (b) corresponding Tauc plot of CdS sample.

spectra, XPS, and ICP-OES. Firstly, the successful acquisition of Ti_3C_2 and CdS was verified by the XRD patterns. As represented in Fig. 1a, the Ti_3AlC_2 precursor exhibited its XRD diffraction peaks at 9.7°, 19.1° and 39.1°, corresponding to the (002), (004) and (104) lattice planes (JCPDS No. 52–0875), respectively [46,47]. After etching by the HCl+HF+LiF mixture, it was obvious that the strongest peak at 39.1° for the Al layer disappeared in the XRD pattern of Ti_3C_2, and the (002) diffraction peak shifted from 9.7° to 7.1°, which verified the successful erosion of the Al layer in Ti_3AlC_2 and the formation of Ti_3C_2 with a large interlayer spacing [44,48]. The XRD pattern of the TM9 sample showed little difference from that of the Ti_3C_2 due to the low content and uniform distribution of MoS_2 [28]. It also indicated that the growth of MoS_2 had no effect on the structure of Ti_3C_2. The existence of MoS_2 in the TM9 sample would be identified by Raman spectra and XPS as discussed later.

For CdS and its composites, the XRD patterns exhibited main diffraction peaks at 24.9°, 26.5°, 28.2°, 43.8°, 47.7° and 51.9°, belonging to the (100), (002), (101), (110), (103), and (112) lattice planes of hexagonal CdS (JCPDS NO. 41–1049), respectively (Fig. 1b) [49,50]. In the binary CT1.5 and ternary C(TM9)x samples, the diffraction peaks of MoS_2 and Ti_3C_2 were not discovered due to the their low content.

To verify the presence of MoS_2 in the composite, the vibrational modes of bare Ti_3C_2 and TM9 were investigated by Raman spectroscopy (Fig. 2a). For bare Ti_3C_2 sample, the typical peaks at 204, 291, 448 and 592 cm^{-1} were originated from ω_1, ω_2, ω_3, and ω_4 Raman-active phonon vibration mode of nonstoichiometric Ti_3C_2, and two broad peaks at 1478 and 1598 cm^{-1} were accounted for D and G bands of graphitic carbon in Ti_3C_2, respectively [10,51]. Compared to Ti_3C_2, two characteristic Raman peaks appeared at 382 and 405 cm^{-1} for the TM9 sample, which could be assigned to the vibrational modes of E^1_{2g} and $A_{1\,g}$ of MoS_2, respectively [29,52]. Furthermore, the presence of MoS_2 in TM9 and its element valence states were characterized by XPS. In the high resolution XPS spectra of the TM9 sample, two typical peaks centered at 229.8 and 232.8 eV were attributed to Mo $3d_{5/2}$ and Mo $3d_{3/2}$ of Mo^{4+}, respectively (Fig. 2b), while two characteristic peaks at 162.2 and 163.5 eV refers to S $2p_{3/2}$ and S $2p_{1/2}$ of S^{2-}, respectively (Fig. 2c) [29,53]. These results validated that $(NH_4)_2MoS_4$ was successfully reduced into MoS_2 and deposited on the surface of Ti_3C_2 nanosheets.

The actual mass ratio of Ti_3C_2, MoS_2 and CdS in the composites was quantitatively analyzed by ICP-OES. In the TM9 sample, the content of MoS_2 accounts for 8.49 wt.% of Ti_3C_2, which was close to the theoretical value of 9%. It further proved that MoS_2 could be well grown on the surface of Ti_3C_2 by self-reduction without noticeable drain. In the CT1.5 sample, the actual mass percentage of Ti_3C_2 to CdS was 1.43%, which was also approximate to the theoretical value of 1.5%. On the other hand, in the ternary C(TM9)1.5 composite, the Ti_3C_2 and MoS_2 accounted for 0.95% and 0.08% of CdS, respectively, which slightly less

than the theoretical values of 1.5% and 0.135%. It meant that most TM9 nanosheets were successfully combined with CdS nanoparticles during the hydrothermal process, although some CdS nanoparticles were inevitably ex situ formed in the solution.

3.2. Morphological structure

The morphological structure of the samples was characterized by TEM, FESEM and HAADF-STEM. As shown in Fig. 3a, the synthesized Ti_3C_2 by the freeze-and-thaw method displayed as ultrathin nanosheets with a flat and smooth surface. After depositing MoS_2, the surface of Ti_3C_2 nanosheets became rough with dense little pieces (Fig. 3b). The diameter of these irregular MoS_2 nanoparticles was around 20–50 nm. For the bare CdS sample, many nanoparticles with diameters of about 20–100 nm were seriously agglomerated with each other to form cauliflower-like aggregates (Fig. 3c). In comparison, in the C(TM9)1.5 sample, the composite still showed a laminated structure, and the agglomeration phenomenon of CdS nanoparticles seemed to be effectively limited (Fig. 3d), which could be attributed to the presence of Ti_3C_2 as a good 2D substrate. The TEM image of the C(TM9)1.5 sample further displayed that CdS nanoparticles were well dispersed on the surface of ultra-thin Ti_3C_2 nanosheets (Fig. 3e). Its locally amplified HRTEM image (Fig. 3f) described the lattice spacing of 0.34, 0.23 and 0.36 nm, which could be ascribed to the CdS (002), Ti_3C_2 (103), and MoS_2 (004) crystal facets, respectively[10,27,39]. Moreover, the intimate contact of Ti_3C_2, MoS_2, and CdS in the ternary C(TM9)1.5 as well as their position relationship were further well confirmed by the HAADF-STEM image and the EDS elemental mapping images of Cd, S, Mo, and Ti atoms (Fig. 3j).

3.3. Optical absorption property

The effect of cocatalyst loading on the optical absorption property of CdS was studied by UV–vis DRS. As shown in Fig. 4a, the absorption edge of pure CdS was located around 560 nm. After converting the UV–vis DRS curve into the Tauc plot as displayed in Fig. 4b [54,55], the band gap of CdS was calculated to be ca. 2.31 eV. With the introduction of Ti_3C_2 and MoS_2, the absorption edge position of CdS basically remained unchanged, but the light absorption capability in the visible region was apparently improved, which might bring about photothermal effect and promote the photocatalysis reaction to a certain degree [35,56].

3.4. Photocatalytic performance

The photocatalytic performance of the samples was evaluated by testing their visible-light H_2 evolution reaction (HER) activities in the LA
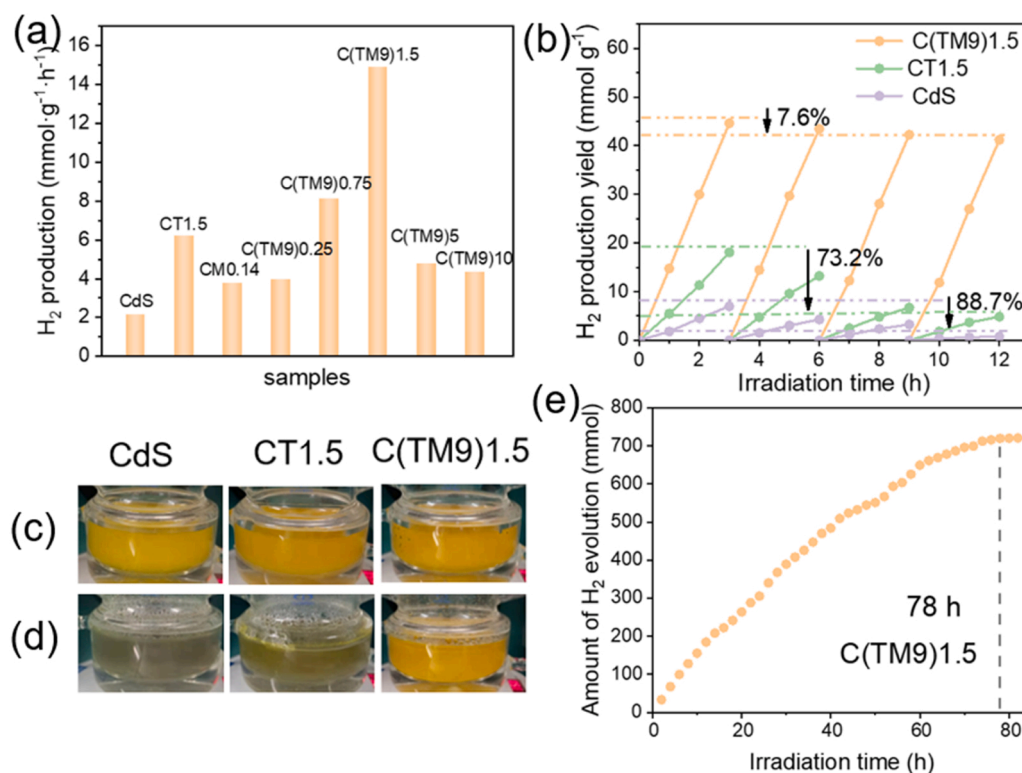
Fig. 5. (a) Comparison of the photocatalytic H₂ production rates of CdS, CT1.5, CM0.14 and C(TM9)x samples. (b) Cycling activity test and the photographs of (c) original H₂-production solutions and (d) H₂-production solutions after 4-hours illumination for CdS, CT1.5 and C(TM9)1.5 samples. (e) Time-dependent photocatalytic H2 production profile of the C(TM9)1.5 sample.

aqueous solution (10 vol.%), where the LA was used as the sacrificial agent. The comparison of the average H₂ production rates of the bare CdS, binary CT1.5, CM0.14 and ternary C(TM9)x samples after four-hour irradiation was shown in Fig. 5a. Typically, the original CdS exhibited the lowest photoactivity of only 2.18 mmol·h^{-1}·g^{-1}. After adding single cocatalyst, the photocatalytic H₂ production rates of the binary CT1.5 and CM0.14 samples increased to be 6.21 and 3.80 mmol·h^{-1}·g^{-1}, respectively, and the co-modification of MoS₂ and Ti₃C₂ further offered the ternary sample with even higher performance. Especially, the H₂ production rate of the C(TM9)1.5 sample achieved the highest as 14.88 mmol·h^{-1}·g^{-1}, which was 6.8 times higher than that of pure CdS. Obviously, it was the synergistic effect of dual co-catalysts Ti₃C₂/MoS₂ that significantly enhanced the photocatalytic performance of CdS. However, overburdened cocatalysts led to the decreased activity. For example, the H₂ production rate of the C(TM9)10 sample retrogressed to be 4.37 mmol·h^{-1}·g^{-1}, even lower than the CT1.5

sample. It is because excessive MoS₂/Ti₃C₂ cocatalyst with dark color would bring about a "shielding effect" to block the light absorption of CdS, and also prevent some active sites on the surface of CdS [57].

For semiconductor photocatalysts, the photostability is as important as its photoactivity in terms of future practical application. Therefore, the cycling activity tests were carried out over the C(TM9)1.5 sample to evaluate its photostability, using bare CdS and CT1.5 as the reference samples. As shown in Fig. 5b, the photoactivity of bare CdS severely decreased by 88.7% after four cycles within the total irradiation time of 12 h. When Ti₃C₂ was loaded, the activity decline of the CT1.5 sample (by 73.2%) was slowed down for a little bit. However, with the co-loading of MoS₂ and Ti₃C₂, the photoactivity of the C(TM9)1.5 sample decreased only by 7.6% after four cycles. More obvious difference among the three samples could be found by direct observing their color change before and after the H₂ production process. As shown in Fig. 5c, all of the original sample suspensions displayed a color of orange yellow
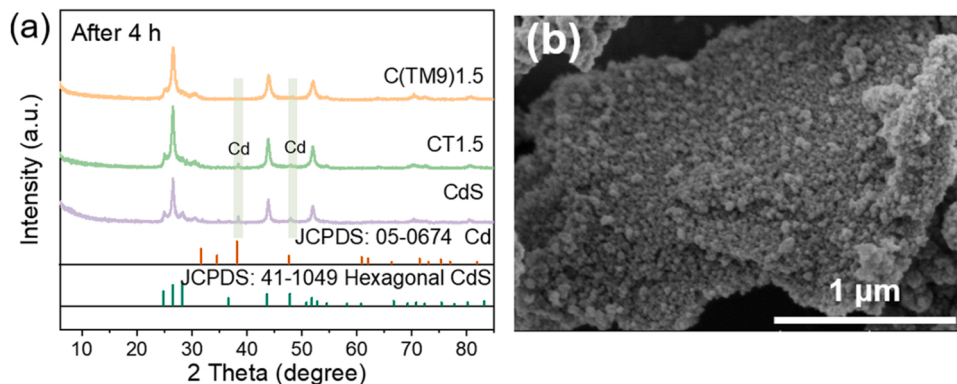

Fig. 6. (a) XRD patterns of the CdS, CT1.5 and C(TM9)1.5 samples after four-hour H₂ production. (b) FESEM images of the C(TM9)1.5 sample after four-hour H₂ production.
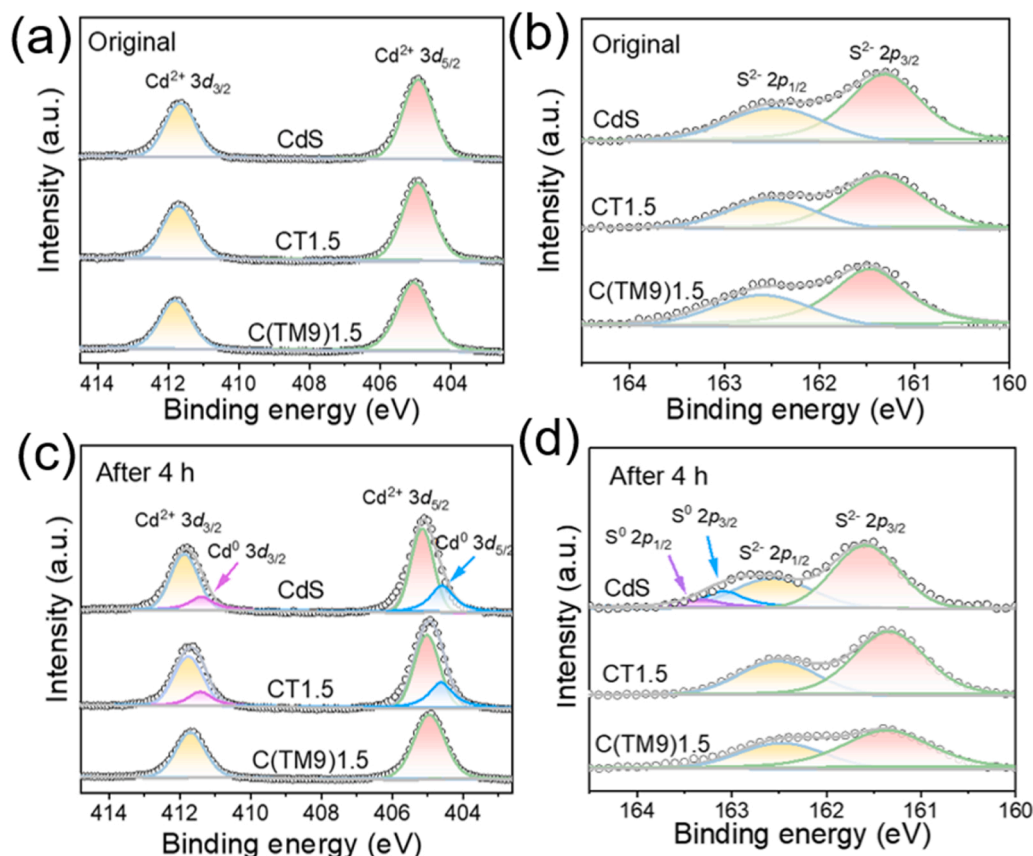
Fig. 7. High-resolution XPS spectra of (a) Cd $3d$ and (b) S $2p$ of original CdS, CT1.5 and C(TM9)1.5. High-resolution XPS spectra of (c) Cd $3d$ and (d) S $2p$ of CdS, CT1.5 and C(TM9)1.5 after 4-hours H_2 production.

before the photocatalytic reaction started. After four-hour light irradiation, it was quite clear that the CdS suspension turned black, the CT1.5 suspension turned brown, and the C(TM9)1.5 suspension remained its orange yellow (Fig. 5d). Combining the results of cycling activity tests with the color change observation, it can be deduced that bare CdS encountered severe photocorrosion and experienced the greatest decrease in activity, and adding Ti_3C_2 only remitted this process by a little bit. Fortunately, simultaneous loading of Ti_3C_2 and MoS_2 could almost completely inhibit the occurrence of photocorrosion over CdS. With prolonging reaction time, the C(TM9)1.5 photocatalyst could even generate H_2 at a constant rate for as long as 78 h (Fig. 5e), during which the suspension stayed yellow all the time.

In order to shed light on the intrinsic change occurred on CdS after coloading with Ti_3C_2 and MoS_2, and explain the different photocorrosion degrees of the samples, XRD, FESEM and XPS were carried out to investigate the components of these samples before and after four-hour illumination. It can be observed that there was no obvious difference between the XRD patterns of the original three samples (Fig. 1b). After four-hour hydrogen production reaction, however, the diffraction peak of metal Cd (JCPDS NO. 05–0674) appeared in bare CdS and CT1.5 [58,59], but not in the C(TM9)1.5 sample (Fig. 6a). This fact reflected that the surface lattice Cd^{2+} in CdS was reduced into metal Cd in the procedure of hydrogen production over the bare CdS and CT1.5 samples, which did not happen over the C(TM9)1.5 sample. Furthermore, the morphology comparison of the C(TM9)1.5 sample before and after four-hour H_2-production reaction, as shown in Fig. 3d and Fig. 6b, respectively, told that the laminated structure of this ternary composite photocatalyst remained stable during the photoreaction.

Moreover, XPS analysis on the Cd and S elements was carefully carried out on the samples before and after four-hour illumination. As a whole, CdS, CT1.5 and C(TM9)1.5 showed similar XPS spectra of Cd and

S before illumination. For CdS, the peaks at 411.7 and 405.0 eV corresponded to Cd $3d_{3/2}$ and Cd $3d_{5/2}$, respectively (Fig. 7a) [14,60], while the peaks at 162.5 and 161.4 eV attributed to S $2p_{1/2}$ and S $2p_{3/2}$, respectively (Fig. 7b) [29,60]. It proved that Cd and S element were in the chemical state of Cd^{2+} and S^{2-} [61,62].

After four-hour illumination, there were some differences in the XPS spectra of the samples as shown in Fig. 7c and d. Obviously, both the new characteristic peaks for Cd^0 (411.4 and 404.6 eV) and S^0 (163.1 and 163.4 eV) could be discovered in CdS, whilst only the new characteristic peaks for Cd^0 in CT1.5 could be found [63]. However, as for C(TM9)1.5, neither metal Cd^0 nor S^0 were found in its XPS spectra after light irradiation. The XPS results were in good agreement with the pivotal discrepancy in the XRD patterns (Figs. 1b and 6a) as well as the suspension colors (Fig. 5c and d) of the samples after light irradiation. As a consequence, it could be verified that the severe photocorrosion of bare CdS was attributed to the redox of surface lattice Cd^{2+} and S^{2-} into Cd^0 and S^0, respectively, and the introduction of Ti_3C_2 into CdS brought about a moderate remission of photocorrosion because only Cd^{2+} was reduced into Cd^0. More importantly, when Ti_3C_2 and MoS_2 were synchronously decorated, both the component and structure of the C(TM9)1.5 sample maintain stable after light irradiation, meaning that CdS was successfully kept clear of photocorrosion.

3.5. Charge transfer mechanism

All the above results comprehensively showed that both photocatalytic activity and stability of CdS were remarkably promoted with the synergistic assistance of Ti_3C_2 and MoS_2 cocatalysts. It is well known that the performance of photocatalysts mainly depends on the generation, separation and transfer efficiency of photoexcited electron-hole pairs. Therefore, a series of photo/electrochemical experiments as well
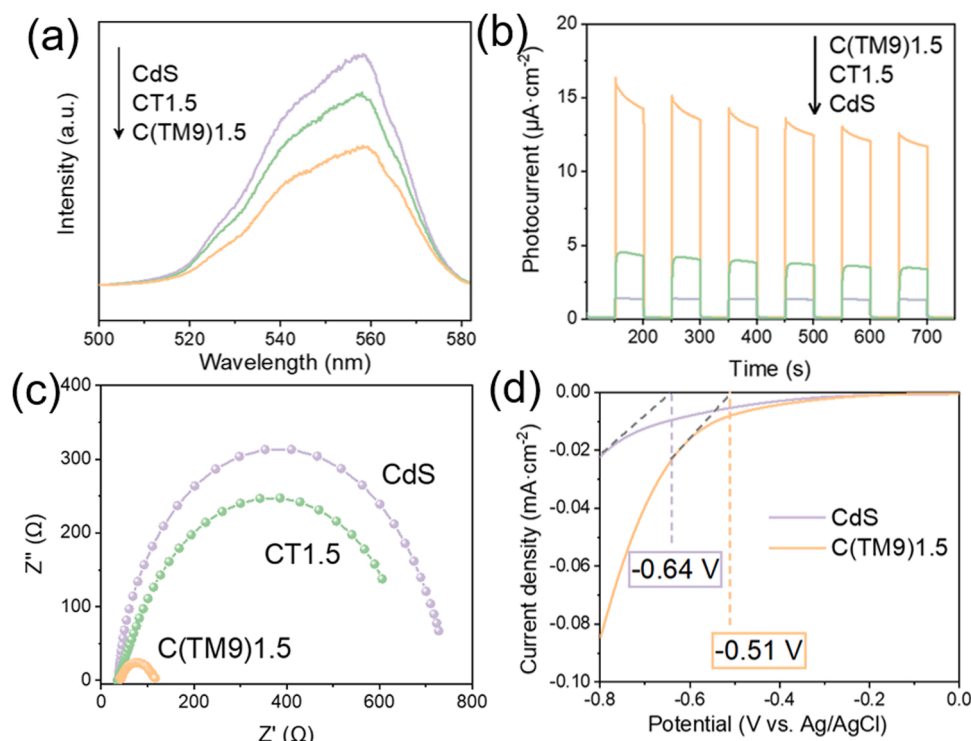
Fig. 8. (a) Steady-state PL spectra, (b) TPR plots and (c) EIS plots of CdS, CT1.5 and C(TM9)1.5 samples. (d) LSV curves of CdS and C(TM9)1.5 samples.

as theoretical calculations over the composite samples were carried out to investigate the underlying promotion mechanism.

Firstly, PL emission spectra, TPR and EIS were conducted to determine the important contribution of carrier separation efficiency on the improvement of photocatalytic performance. Among them, the PL spectra (λ_{Ex} = 270 nm) were used to analyze the recombination efficiency of photogenerated charge carriers of CdS in the different samples. It is generally believed that when the photo-induced electrons recombined with holes, the generated energy was emitted in the form of fluorescence [64]. Therefore, lower fluorescent intensity meant lower recombination rate of electron-hole pairs, which was a desirable optical property for excellent photocatalysts. As shown in Fig. 8a, all the three samples of CdS, CT1.5 and C(TM9)1.5 exhibited a distinct PL emission peak at 557 nm, which was attributed to the band edge emission of CdS. This fact was in line with the test results of DRS (Fig. 4a). Compared with pristine CdS and CT1.5, the C(TM9)1.5 composite showed the lowest fluorescence intensity. It was because the interfacial coupling between CdS and Ti_3C_2/MoS_2 effectively promoted the charge transfer kinetics of CdS to suppress the recombination of photogenerated charges, thereby offering the ternary composite with outstanding charge separation efficiency and excellent photocatalytic H_2 production efficiency.

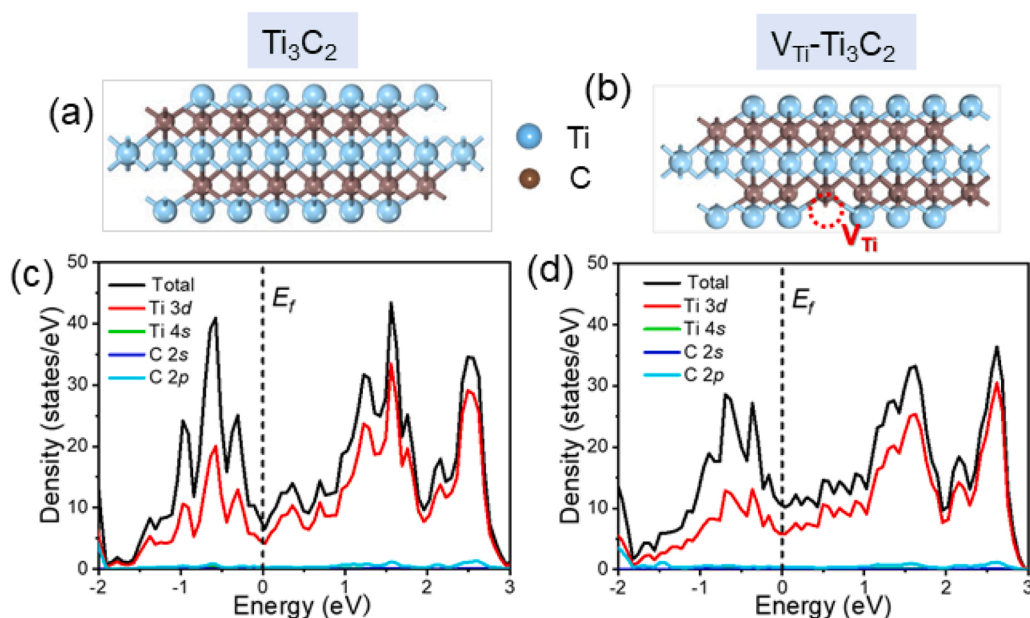The fact that Ti_3C_2 and MoS_2 as dual cocatalysts could effectively

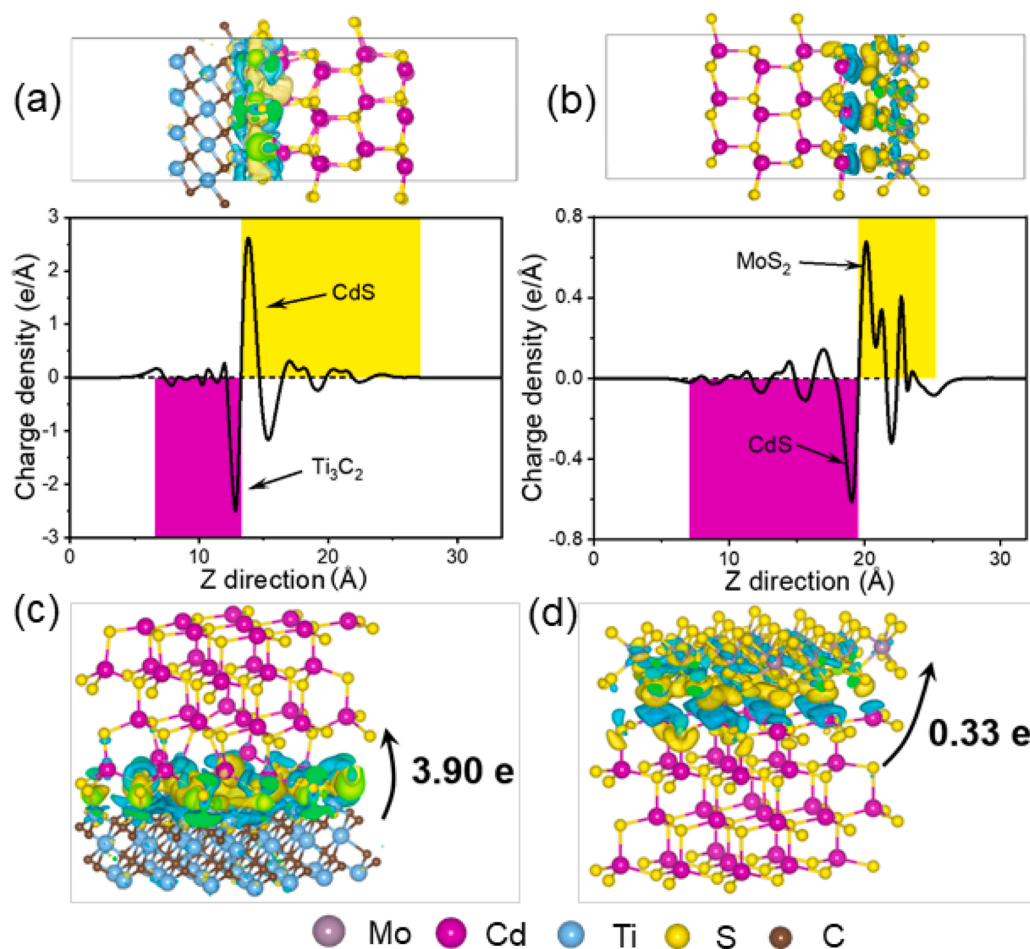**Fig. 9.** (a, b) Structure models and (c, d) density of states of Ti_3C_2 and V_{Ti}-Ti_3C_2.

Fig. 10. (a, b) Electron density difference (8×10^{-4} e/Å^3) and (c,d) Bader electron transfer at the CdS/V_{Ti}-Ti$_3$C$_2$ and CdS/MoS$_2$ interfaces.

improve the separation efficiency of photo-induced charge carriers was further confirmed by TPR and EIS analysis. According to Fig. 8b, the photocurrent density of the C(TM9)1.5 sample was much stronger than that of pure CdS, suggesting that the recombination of electron-hole pairs were successfully inhibited. Thus, sufficient photogenerated electrons could be involved in the proton reduction reaction. In addition, the arc diameter of C(TM9)1.5 in the EIS Nyquist plots was the smallest among the samples (Fig. 8c). It meant that it had a lower resistance value, which was more conducive to charge transfer. Based on the above analysis, the C(TM9)1.5 composite exhibited the lowest rate of electron-hole recombination and the fastest efficiency of charge separation and transfer among all the samples. Therefore, it showed the highest H$_2$ production performance.

The photocatalytic H$_2$ generation activity was also highly dependent on the hydrogen evolution reaction (HER) overpotential during the reaction. The smaller the overpotential, the more favorable for H$_2$ production. According to the LSV testing result, the overpotential of C(TM9)1.5 (−0.51 V vs. Ag/AgCl at pH = 5.45) was smaller than that of CdS (−0.64 V vs. Ag/AgCl at pH = 5.45), which further confirmed that C(TM9)1.5 was a suitable photocatalyst for H$_2$ production (Fig. 8d) [65, 66].

Moreover, in order to further confirm the charge transfer mechanism at the interfaces of CdS/Ti$_3$C$_2$ and CdS/MoS$_2$, theoretical calculations were explored based on the density functional theory (DFT). Firstly, given the existence of Ti vacancies in Ti$_3$C$_2$, the density of states (DOS) calculations were implemented to analyze the effect of Ti vacancies on its electronic structure. The structural models of intact Ti$_3$C$_2$ and defective Ti$_3$C$_2$ (V_{Ti}-Ti$_3$C$_2$) were developed in Fig. 9a and b, respectively. The DOS of both Ti$_3$C$_2$ and V_{Ti}-Ti$_3$C$_2$ were continuous near the Fermi

level, signifying the excellent conductivity of them (Fig. 9c and d) [10]. It is worthy to note that V_{Ti}-Ti$_3$C$_2$ exhibited an increased DOS at the Fermi level in contrast with Ti$_3$C$_2$, which reflected that the presence of Ti vacancies were beneficial to enhance the electronic conductivity of Ti$_3$C$_2$ [67].

Furthermore, the charge-transfer directions and numbers were elucidated by the electron density difference and Bader charge analysis, respectively. As shown in Fig. 10a and c, the charge redistribution mainly occurred near the interface of CdS/MoS$_2$ and CdS/V_{Ti}-Ti$_3$C$_2$, which indicated that CdS was intimately bound with MoS$_2$ and Ti$_3$C$_2$ and had a strong interaction with each other. The yellow area represented the charge accumulation, and the cyan area represented the charge depletion. The plane average charge density difference along the Z direction was plotted to directly reflect the charge density change, which told that electrons were inclined to transfer from Ti$_3$C$_2$ to CdS at the CdS/V_{Ti}-Ti$_3$C$_2$ interface, while electrons preferred to transfer from CdS to MoS$_2$ at the CdS/MoS$_2$ interface. In addition, Bader charge analysis was calculated to tell the specific charge transfer number. As shown in the Fig. 10c and d, the electrons transferred from Ti$_3$C$_2$ to CdS and from CdS to MoS$_2$ were 3.90 e and 0.33 e, respectively. The theoretical calculation results meant that, when Ti$_3$C$_2$ was loaded on CdS, the photogenerated holes on CdS would rapidly transfer to Ti$_3$C$_2$ to alleviate the photocorrosion caused by S^{2-} oxidation, which well explained the absence of S^0 in the XPS spectra of the illuminated CT1.5 samples (Fig. 7d). When Ti$_3$C$_2$ and MoS$_2$ were co-loaded on CdS, the photogenerated holes and electrons respectively transferred to Ti$_3$C$_2$ and MoS$_2$, which well elucidated the consequence that both Cd^0 and S^0 were not observed in the illuminated C(TM9)1.5 sample (Figs. 6 and 7). As a result, the co-loading of MoS$_2$/Ti$_3$C$_2$ can not only promote the
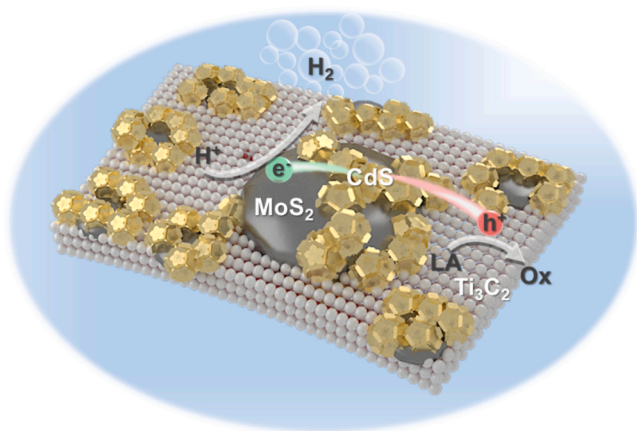
Fig. 11. Proposed mechanism of charge transfer over ternary CdS@MoS$_2$/Ti$_3$C$_2$ photocatalysts during photocatalytic H$_2$ evolution, where LA refers to lactic acid as the sacrificial agent.

separation of photogenerated charge carriers, but also effectively avoided the photocorrosion, guaranteeing the ternary C(TM9)1.5 composite with excellent photocatalytic performance and stability.

Based on the above analysis, a reasonable charge transfer mechanism was proposed as illustrated in Fig. 11. Under visible-light illumination, the photogenerated electrons and holes from CdS would respectively reduce protons (H$^+$) to generate H$_2$ and oxidize LA on its surface. However, pure CdS nanoparticles tend to agglomerate with each other, so that the active sites were obscured, and the recombination rates of photogenerated charge carriers were undesirably high. After the introduction of MoS$_2$ and Ti$_3$C$_2$, the photo-generated holes and electrons on the surface of CdS rapidly transferred to Ti$_3$C$_2$ and MoS$_2$, respectively. As a result, the hole-electron pair can be effectively separated, providing more charges to participate in the subsequent redox reactions. More importantly, the occurrence of photocorrosion was effectively avoided, and the component and structure of the catalyst was remarkably remained. Therefore, under the synergistic effect of dual cocatalysts, the ternary CdS@MoS$_2$/Ti$_3$C$_2$ composite exhibited both wonderful performance and prominent stability.

4. Conclusion

In a word, we made use of the reductive Ti vacancies of 2D Ti$_3$C$_2$ MXene to prepare the MoS$_2$/Ti$_3$C$_2$ composite, and further induced the in-situ growth of CdS on its surface, elaborately constructing the ternary CdS@MoS$_2$/Ti$_3$C$_2$ composites with intimate binding interface. The series of fabricated composites were applied to produce H$_2$ from photocatalytic water splitting under visible-light irradiation. Among the samples, the H$_2$ production rate of C(TM9)1.5 reached the maximum as 14.88 mmol·h^{-1}·g^{-1}, which was 6.8 times of that of bare CdS. More importantly, the lifetime of the C(TM9)1.5 sample for H$_2$ production was as long as 78 h, without obvious change in its color and structure, which meant that the photocorrosion usually occurred on CdS was effectively inhibited. The experimental and theoretical results comprehensively illustrated that Ti$_3$C$_2$ and MoS$_2$ played vital roles in trapping holes and electrons, respectively. Such charge transfer route not only effectively prevented the recombination of photogenerated hole-electron pairs, making it possible that more available electrons took part in H$_2$ production reaction, but also inhibited the appearance of photocorrosion on CdS, leading to excellent photostability. The co-modification of redox cocatalysts insures the catalytic activity and durability of the photocatalyst, which might help bridge the translational gap in photocatalytic technologies and practical applications in the future.

CRediT authorship contribution statement

Chao Wu: Data curation, Investigation, Writing-original draft; Weixin Huang: Data curation, Investigation, Writing-original draft; Huanmin Liu: Visualization, Validation; Kangle Lv: Supervision, Validation; Qin Li: Conceptualization, Supervision, Writing - review & editing, Funding acquisition.

Declaration of Competing Interest

The authors declare that they have no known competing financial interests or personal relationships that could have appeared to influence the work reported in this paper.

Data Availability

Data will be made available on request.

References

[1] S.B. Wang, Y. Wang, S.L. Zhang, S.Q. Zang, X.W.D. Lou, Supporting ultrathin ZnIn$_2$S$_4$ nanosheets on Co/N-doped graphitic carbon nanocages for efficient photocatalytic H$_2$ generation, Adv. Mater. 31 (2019), 1903404.

[2] G. Zuo, Y. Wang, W.L. Teo, A. Xie, Y. Guo, Y. Dai, W. Zhou, D. Jana, Q. Xian, W. Dong, Y. Zhao, Ultrathin ZnIn$_2$S$_4$ nanosheets anchored on Ti$_3$C$_2$T$_x$ MXene for photocatalytic H$_2$ evolution, Angew. Chem. Int. Ed. 59 (2020) 11287–11292.

[3] S. Wang, B.Y. Guan, X. Wang, X.W.D. Lou, Formation of hierarchical Co$_9$S$_8$@ ZnIn$_2$S$_4$ heterostructured cages as an efficient photocatalyst for hydrogen evolution, J. Am. Chem. Soc. 140 (2018) 15145–15148.

[4] Y. Liu, W. Yang, Q. Chen, D.A. Cullen, Z. Xie, T. Lian, Pt particle size affects both the charge separation and water reduction efficiencies of CdS-Pt nanorod photocatalysts for light driven H$_2$ generation, J. Am. Chem. Soc. 144 (2022) 2705–2715.

[5] C. Chen, W.Q. Hou, Y.M. Xu, Significantly increased production of H$_2$ on ZnIn$_2$S$_4$ under visible light through co-deposited CoWO$_4$ and Co$_3$O$_4$, Appl. Catal. B Environ. 316 (2022), 121676.

[6] C.L. Tan, M.Y. Qi, Z.R. Tang, Y.J. Xu, Cocatalyst decorated ZnIn$_2$S$_4$ composites for cooperative alcohol conversion and H$_2$ evolution, Appl. Catal. B Environ. 298 (2021), 120541.

[7] K.Q. Lu, M.Y. Qi, Z.R. Tang, Y.J. Xu, Earth-abundant MoS$_2$ and cobalt phosphate dual cocatalysts on 1D CdS nanowires for boosting photocatalytic hydrogen production, Langmuir 35 (2019) 11056–11065.

[8] Y. Liu, Y.H. Li, X. Li, Q. Zhang, H. Yu, X. Peng, F. Peng, Regulating electron-hole separation to promote photocatalytic H$_2$ evolution activity of nanoconfined Ru/ MXene/TiO$_2$ catalysts, ACS Nano 14 (2020) 14181–14189.

[9] Y.J. Li, Y.Y. Liu, D.N. Xing, J.J. Wang, L.R. Zheng, Z.Y. Wang, P. Wang, Z.K. Zheng, H.F. Cheng, Y. Dai, B.B. Huang, 2D/2D heterostructure of ultrathin BiVO$_4$/Ti$_3$C$_2$ nanosheets for photocatalytic overall water splitting, Appl. Catal. B Environ. 285 (2021), 119855.

[10] Z.P. Li, W.X. Huang, J.X. Liu, K.L. Lv, Q. Li, Embedding CdS@Au into ultrathin Ti$_{3-x}$C$_2$T$_y$ to build dual schottky barriers for photocatalytic H$_2$ production, ACS Catal. 11 (2021) 8510–8520.

[11] S. Iqbal, Z. Pan, K. Zhou, Enhanced photocatalytic hydrogen evolution from in situ formation of few-layered MoS$_2$/CdS nanosheet-based van der Waals heterostructures, Nanoscale 9 (2017) 6638–6642.

[12] T. Tian, X.Y. Jin, N. Guo, H.Q. Li, Y. Han, Y.P. Yuan, CdS/ethylenediamine nanowires 3D photocatalyst with rich sulfur vacancies for efficient syngas production from CO$_2$ photoreduction, Appl. Catal. B Environ. 308 (2022), 121227.

[13] J.X. Lv, Z.M. Zhang, J. Wang, X.L. Lu, W. Zhang, T.B. Lu, In situ synthesis of CdS/ graphdiyne heterojunction for enhanced photocatalytic activity of hydrogen production, ACS Appl. Mater. Interfaces 11 (2019) 2655–2661.

[14] Y. Yang, D. Zhang, Q. Xiang, Plasma-modified Ti$_3$C$_2$T$_x$/CdS hybrids with oxygen-containing groups for high-efficiency photocatalytic hydrogen production, Nanoscale 11 (2019) 18797–18805.

[15] Y. Zhao, C. Shao, Z. Lin, S. Jiang, S. Song, Low-energy facets on CdS allomorph junctions with optimal phase ratio to boost charge directional transfer for photocatalytic H$_2$ fuel evolution, Small 16 (2020), 2000944.

[16] X.F. Ning, J. Li, B.J. Yang, W.L. Zhen, Z. Li, B. Tian, G.X. Lu, Inhibition of photocorrosion of CdS via assembling with thin film TiO$_2$ and removing formed oxygen by artificial gill for visible light overall water splitting, Appl. Catal. B Environ. 212 (2017) 129–139.

[17] H.G. Yu, W. Zhong, X. Huang, P. Wang, J.G. Yu, Suspensible cubic-phase cds nanocrystal photocatalyst: Facile synthesis and highly efficient H$_2$-evolution performance in a sulfur-rich system, ACS Sustain. Chem. Eng. 6 (2018) 5513–5523.

[18] X.F. Ning, G.X. Lu, Photocorrosion inhibition of CdS-based catalysts for photocatalytic overall water splitting, Nanoscale 12 (2020) 1213–1223.

[19] Y. Chen, W. Zhong, F. Chen, P. Wang, J. Fan, H. Yu, Photoinduced self-stability mechanism of CdS photocatalyst: the dependence of photocorrosion and H$_2$-evolution performance, J. Mater. Sci. Technol. 121 (2022) 19–27.

[20] F.J. Chen, X.K. Jin, D.Z. Jia, Y.L. Cao, H.M. Duan, M.Q. Long, Efficient treament of organic pollutants over CdS/graphene composites photocatalysts, Appl. Surf. Sci. 504 (2020), 144422.

[21] C. Bie, B. Zhu, L. Wang, H. Yu, C. Jiang, T. Chen, J. Yu, A bifunctional CdS/MoO$_2$/MoS$_2$ catalyst enhances photocatalytic H$_2$ evolution and pyruvic acid synthesis, Angew. Chem. Int. Ed. 61 (2022), 202212045.

[22] B.T. Sun, P.Y. Qiu, Z.Q. Liang, Yj Xue, X. Zhang, L. Yang, H. Cui, J. Tian, The fabrication of 1D/2D CdS nanorod@Ti$_3$C$_2$ MXene composites for good photocatalytic activity of hydrogen generation and ammonia synthesis, Chem. Eng. J. 406 (2021) 127177.

[23] X. Cheng, Y. Lu, Y.X. Liu, G. Tian, X.Y. Yang, One-pot synthesis of hierarchical CdS/MoS$_2$/rGO with enhanced (photo) electrocatalytic activities, Chem. Phys. Lett. 759 (2020), 138047.

[24] B. He, C. Bie, X. Fei, B. Cheng, J. Yu, W. Ho, A.A. AlGhamdi, S. Wageh, Enhancement in the photocatalytic H$_2$ production activity of CdS NRs by Ag$_2$S and NiS dual cocatalysts, Appl. Catal. B Environ. 288 (2021), 119994.

[25] Z.Z. Liang, R.C. Shen, Y.H. Ng, P. Zhang, Q.J. Xiang, X. Li, A review on 2D MoS$_2$ cocatalysts in photocatalytic H$_2$ production, J. Mater. Sci. Technol. 56 (2020) 89–121.

[26] Y.J. Li, L. Ding, Z.Q. Liang, Y.J. Xue, H.Z. Cui, J. Tian, Synergetic effect of defects rich MoS$_2$ and Ti$_3$C$_2$ MXene as cocatalysts for enhanced photocatalytic H$_2$ production activity of TiO$_2$, Chem. Eng. J. 383 (2020), 123178.

[27] J. Yang, Q.X. Zhu, Z.G. Xie, Y.J. Wang, J.K. Wang, Y. Peng, Y.Y. Fang, L.H. Deng, T. P. Xie, L.J. Xu, Enhancement mechanism of photocatalytic activity for MoS$_2$/Ti$_3$C$_2$ schottky junction: experiment and DFT calculation, J. Alloy. Compd. 887 (2021).

[28] B. Han, S.Q. Liu, N. Zhang, Y.J. Xu, Z.R. Tang, One-dimensional CdS@MoS$_2$ core-shell nanowires for boosted photocatalytic hydrogen evolution under visible light, Appl. Catal. B Environ. 202 (2017) 298–304.

[29] D. Ma, Q.F. Lu, E. Guo, F. Tao, M. Wei, CdS/MoS$_2$ nanoparticles on nanoribbon heterostructures with boosted photocatalytic H$_2$ evolution under visible-light irradiation, ChemistrySelect 6 (2021) 2561–2568.

[30] S.Q. Zhang, X. Liu, C.B. Liu, S.L. Luo, L.L. Wang, T. Cai, Y.X. Zeng, J.L. Yuan, W. Y. Dong, Y. Pei, Y.T. Liu, MoS$_2$ quantum dot growth induced by S vacancies in a ZnIn$_2$S$_4$ monolayer: Atomic-level heterostructure for photocatalytic hydrogen production, ACS Nano 12 (2018) 751–758.

[31] Q. Liu, S. Wang, Q. Ren, T. Li, G. Tu, S. Zhong, Y. Zhao, S. Bai, Stacking design in photocatalysis: synergizing cocatalyst roles and anti-corrosion functions of metallic MoS$_2$ and graphene for remarkable hydrogen evolution over CdS, J. Mater. Chem. A 9 (2021) 1552–1562.

[32] H. Zhao, Y.M. Dong, P.P. Jiang, H.Y. Miao, G.L. Wang, J. Zhang, In situ light-assisted preparation of MoS$_2$ on graphitic C$_3$N$_4$ nanosheets for enhanced photocatalytic H$_2$ production from water, J. Mater. Chem. A 3 (2015) 7375–7381.

[33] B. Wang, M.Y. Wang, F.Y. Liu, Q. Zhang, S. Yao, X.L. Liu, F. Huang, Ti$_3$C$_2$: an ideal co-catalyst? Angew. Chem. Int. Ed. 59 (2020) 1914–1918.

[34] K.N. Li, S.S. Zhang, Y.H. Li, J.J. Fan, K.L. Lv, MXenes as noble-metal-alternative co-catalysts in photocatalysis, Chin. J. Catal. 42 (2021) 3–14.

[35] R. Li, L. Zhang, L. Shi, P. Wang, MXene Ti$_3$C$_2$: an effective 2D light-to-heat conversion material, ACS Nano 11 (2017) 3752–3759.

[36] D. Singh, V. Shukla, N. Khossossi, A. Ainane, R. Ahuja, Harnessing the unique properties of MXenes for advanced rechargeable batteries, J. Phys. -Energy 3 (2020), 012005.

[37] Y. Gao, C. Yan, H. Huang, T. Yang, G. Tian, D. Xiong, N. Chen, X. Chu, S. Zhong, W. Deng, Y. Fang, W. Yang, Microchannel-confined Mxene based flexible piezoresistive multifunctional micro-force sensor, Adv. Mater. 30 (2020), 1909603.

[38] F. Shahzad, M. Alhabeb, C.B. Hatter, B. Anasori, S.M. Hong, C. Min Koo, Y. Gogotsi, Electromagnetic interference shielding with 2D transition metal carbides (MXenes), Science 353 (2016) 1137–1140.

[39] W.X. Huang, Z.P. Li, C. Wu, H.J. Zhang, J. Sun, Q. Li, Delaminating Ti$_3$C$_2$ MXene by blossom of ZnIn$_2$S$_4$ microflowers for noble-metal-free photocatalytic hydrogen production, J. Mater. Sci. Technol. 120 (2022) 89–98.

[40] R. Xiao, C.X. Zhao, Z.Y. Zou, C. Chen, L. Tian, H. Xu, H. Tang, Q. Liu, Z. Lin, X. Yang, In situ fabrication of 1D CdS nanorod/2D Ti$_3$C$_2$ MXene nanosheet Schottky heterojunction toward enhanced photocatalytic hydrogen evolution, Appl. Catal. B Environ. 268 (2020), 118382.

[41] D. Zhao, Z. Chen, W. Yang, S. Liu, X. Zhang, Y. Yu, W.C. Cheong, L. Zheng, F. Ren, G. Ying, Y. Cao, D. Wang, Q. Peng, G. Wang, C. Chen, MXene (Ti$_3$C$_2$) vacancy-confined single-atom catalyst for efficient functionalization of CO$_2$, J. Am. Chem. Soc. 141 (2019) 4086–4093.

[42] C. Peng, P. Wei, X. Li, Y. Liu, Y. Cao, H. Wang, H. Yu, F. Peng, L. Zhang, B. Zhang, K.L. Lv, High efficiency photocatalytic hydrogen production over ternary Cu/TiO$_2$@Ti$_3$C$_2$T$_x$ enabled by low-work-function 2D titanium carbide, Nano Energy 53 (2018) 97–107.

[43] J.X. Yang, W.B. Yu, C.F. Li, W.D. Dong, L.Q. Jiang, N. Zhou, Z.P. Zhuang, J. Liu, Z. Y. Hu, H. Zhao, Y. Li, L. Chen, J. Hu, B.L. Su, PtO nanodots promoting Ti$_3$C$_2$ MXene in-situ converted Ti$_3$C$_2$/TiO$_2$ composites for photocatalytic hydrogen production, Chem. Eng. J. 420 (2021), 129695.

[44] X.W. Huang, P.Y. Wu, A Facile, high-yield, and freeze-and-thaw-assisted approach to fabricate mxene with plentiful wrinkles and its application in on-chip micro-supercapacitors, Adv. Funct. Mater. 30 (2020), 1910048.

[45] X. Li, Z. Wang, J. Zhang, K. Dai, K. Fan, G. Dawson, Branch-like Cd$_x$Zn$_{1−x}$Se/Cu$_2$O@Cu step-scheme heterojunction for CO$_2$ photoreduction, Mater. Today Phys. 26 (2022).

[46] T.S. Mathis, K. Maleski, A. Goad, A. Sarycheva, M. Anayee, A.C. Foucher, K. Hantanasirisakul, C.E. Shuck, E.A. Stach, Y. Gogotsi, Modified Max phase synthesis for environmentally stable and highly conductiveTi$_3$C$_2$ MXene, ACS Nano 15 (2021) 6420–6429.

[47] J.Z. Zhang, N. Kong, S. Uzun, A. Levitt, S. Seyedin, P.A. Lynch, S. Qin, M.K. Han, W.R. Yang, J.Q. Liu, X.G. Wang, Y. Gogotsi, J.M. Razal, Scalable manufacturing of free-standing, strong Ti$_3$C$_2$T$_x$ MXene films with outstanding conductivity, Adv. Mater. 32 (2020), 2001093.

[48] Y. Liao, J. Qian, G. Xie, Q. Han, W. Dang, Y. Wang, L. Lv, S. Zhao, L. Luo, W. Zhang, H.-Y. Jiang, J. Tang, 2D-layered Ti$_3$C$_2$ MXenes for promoted synthesis of NH$_3$ on P25 photocatalysts, Appl. Catal. B Environ. 273 (2020), 119054.

[49] X. Li, G. Yang, S. Li, N. Xiao, N. Li, Y. Gao, D. Lv, L. Ge, Novel dual co-catalysts decorated Au@HCS@PdS hybrids with spatially separated charge carriers and enhanced photocatalytic hydrogen evolution activity, Chem. Eng. J. 379 (2020), 122350.

[50] D. Xiang, X. Hao, Z. Jin, Cu/CdS/MnO$_x$ nanostructure-based photocatalyst for photocatalytic hydrogen evolution, ACS Appl. Nano Mater. 4 (2021) 13848–13860.

[51] J.X. Low, L.Y. Zhang, T. Tong, B. Shen, J. Yu, TiO$_2$/MXene Ti$_3$C$_2$ composite with excellent photocatalytic CO$_2$ reduction activity, J. Catal. 361 (2018) 255–266.

[52] X. Wang, H. Li, H. Li, S. Lin, W. Ding, X.G. Zhu, Z.G. Sheng, H. Wang, X.B. Zhu, Y. P. Sun, 2D/2D 1T-MoS$_2$/Ti$_3$C$_2$ MXene heterostructure with excellent supercapacitor performance, Adv. Funct. Mater. 30 (2020), 1910302.

[53] K.X. Zhuge, Z.J. Chen, Y.Q. Yang, J. Wang, Y. Shi, Z. Li, In-suit photodeposition of MoS$_2$ onto CdS quantum dots for efficient photocatalytic H$_2$ evolution, Appl. Surf. Sci. 539 (2021), 148234.

[54] Z.W. Zhang, Q.H. Li, X.Q. Qiao, D.F. Hou, D.S. Li, One-pot hydrothermal synthesis of willow branch-shaped MoS$_2$/CdS heterojunctions for photocatalytic H$_2$ production under visible light irradiation, Chin. J. Catal. 40 (2019) 371–379.

[55] Y.Y. Qin, H. Li, J. Lu, Y.H. Feng, F.Y. Meng, C.C. Ma, Y.S. Yan, M.J. Meng, Synergy between van der waals heterojunction and vacancy in ZnIn$_2$S$_4$/g-C$_3$N$_4$ 2D/2D photocatalysts for enhanced photocatalytic hydrogen evolution, Appl. Catal. B Environ. 277 (2020), 119254.

[56] Z. Zhou, Q. Song, B. Huang, S. Feng, C. Lu, Facile fabrication of densely packed Ti$_3$C$_2$ MXene/nanocellulose composite films for enhancing electromagnetic interference shielding and electro-/photothermal performance, ACS Nano 15 (2021) 12405–12417.

[57] Q. Li, B.D. Guo, J.G. Yu, J.R. Ran, B.H. Zhang, H.J. Yan, J.R. Gong, Highly efficient visible-light-driven photocatalytic hydrogen production of CdS-cluster-decorated graphene nanosheets, J. Am. Chem. Soc. 133 (2011) 10878–10884.

[58] L. Shang, B. Tong, H.J. Yu, G.I.N. Waterhouse, C. Zhou, Y.F. Zhao, M. Tahir, L. Z. Wu, C.H. Tung, T.R. Zhang, CdS nanoparticle-decorated Cd nanosheets for efficient visible light-driven photocatalytic hydrogen evolution, Adv. Energy Mater. 6 (2016), 1501241.

[59] Z. Zhao, Y. Xing, H. Li, P. Feng, Z. Sun, Constructing CdS/Cd/doped TiO$_2$ Z-scheme type visible light photocatalyst for H$_2$ production, Sci. China Mater. 61 (2017) 851–860.

[60] C. Deng, F. Ye, T. Wang, X. Ling, L. Peng, H. Yu, K. Ding, H. Hu, Q. Dong, H. Le, Y. Han, Developing hierarchical CdS/NiO hollow heterogeneous architectures for boosting photocatalytic hydrogen generation, Nano Res. 15 (2021) 2003–2012.

[61] B. Qiu, L. Cai, N. Zhang, X. Tao, Y. Chai, A ternary dumbbell structure with spatially separated catalytic sites for photocatalytic overall water splitting, Adv. Sci. 7 (2020), 1903568.

[62] F. Zhao, N. Zhang, H. Li, X. Zhang, Z. Luo, Y. Wang, Photocatalyst with chloroplast-like structure for enhancing hydrogen evolution reaction, Energy Environ. Sci. 5 (2021) 1229–1237.

[63] L. Wei, Z. Guo, X. Jia, Probing photocorrosion mechanism of CdS films and enhancing photoelectrocatalytic activity via cocatalyst, Catal. Lett. 151 (2020) 56–64.

[64] Y. Chen, G. Tian, Z. Ren, K. Pan, Y. Shi, J. Wang, H. Fu, Hierarchical core-shell carbon nanofiber@ZnIn$_2$S$_4$ composites for enhanced hydrogen evolution performance, ACS Appl. Mater. Interfaces 6 (2014) 13841–13849.

[65] T.M. Di, L.Y. Zhang, B. Cheng, J. Yu, J. Fan, CdS nanosheets decorated with Ni@ graphene core-shell cocatalyst for superior photocatalytic H$_2$ production, J. Mater. Sci. Technol. 56 (2020) 170–178.

[66] X.Q. Hao, Y. Hu, Z.W. Cui, J. Zhou, Y. Wang, Z.G. Zou, Self-constructed facet junctions on hexagonal CdS single crystals with high photoactivity and photostability for water splitting, Appl. Catal. B Environ. 244 (2019) 694–703.

[67] W. Wang, H.M. Feng, J.G. Liu, M. Zhang, S. Liu, C. Feng, S.G. Chen, A photocatalyst of cuprous oxide anchored MXene nanosheet for dramatic enhancement of synergistic antibacterial ability, Chem. Eng. J. 386 (2020).